Direct Printing of Helical Metal Arrays by Circularly Polarized Light

Ji-Young Kim,[1,2] Connor McGlothin,[1,2] Minjeong Cha,[2,3] Zechariah J. Pfaffenberger,[4] Emine Sumeyra Turali Emre,[1,2] Wonjin Choi,[1,2] Sanghoon Kim,[1] Julie S. Biteen,[4]* Nicholas A. Kotov[1,2,3,5]*

[1] Department of Chemical Engineering, University of Michigan; Ann Arbor, Michigan 48109, USA
[2] Biointerfaces Institute University of Michigan; Ann Arbor, Michigan 48109, USA
[3] Department of Materials Science and Engineering, University of Michigan; Ann Arbor, Michigan 48109, USA
[4] Department of Chemistry, University of Michigan; Ann Arbor, Michigan 48109, USA
[5] Department of Biomedical Engineering, University of Michigan; Ann Arbor, Michigan 48109, USA

*Corresponding author. Email: jsbiteen@umich.edu, kotov@umich.edu

ABSTRACT: Chiral metasurface with orthogonal nanohelical metal arrays provide strong optical rotation but demands multi-step nanofabrication at low-pressure and/or high-temperature conditions, which is incompatible with many substrates and high-throughput assessment. Submillimeter local photonic patterns with various optical polarization were also hitherto unattainable over the same substrate. Here, we demonstrate direct substrate-tolerant printing of silver nanohelicoids with a locally variable optical activity using circularly polarized light (CPL), producing centimeter-scale chiral metasurface within minutes. The light-illuminated sites on the substrate immersed in an aqueous silver ion solution are activated for heterogeneous nucleation at room temperature. Subsequent CPL-induced asymmetric site-selective deposition and self-assembly of the silver nanoparticles (NPs) sculpt the orthogonal silver helicoids at the interface as one-pot synthesis. The ellipticity and wavelength of the incident photons control the handedness and size of the printed silver helicoids, realizing on-the-fly modulation of optical polarization while printing local patterns. Processing simplicity, high polarization rotation, and fine spatial resolution of the light-driven printing can provide a pathway to the sustainable production of chiral plasmonic metasurfaces, accelerating the development of chiral photonics for health and information technologies.

The strong polarization rotation of transmitted and reflected light by chiral inorganic nanostructures with subwavelength dimensions[1–6] catalyzed their rapid development in the last decade.[7–10] The plasmonic metasurfaces with chirality on the nano- and micrometer scale particularly show high sensitivity to changes in their dielectric environment making them promising materials platforms for biosensing, catalysis, photonics, and information technologies.[11–16] However, the complexity of their production hinders access to these materials

for researchers in multiple disciplines outside the metamaterials community interested in their applications. Currently, subwavelength metal geometries on substrates with three-dimensional (3D) chirality are created primarily by two-photon lithography followed by electroplating of metals and etching by plasma.[12,13,17–19] Other patterning methods include ion/electron beam induced deposition[20–22] and glancing angle deposition.[23–27] All of them involve time-consuming and multi-step nanofabrication at low pressure and/or high temperature condition, which are not common even for high-end microfabrication facilities nor are suitable for high throughput fabrication. Placing the pre-synthesized 3D chiral plasmonic elements on substrate had been also recently suggested as an alternative method using soft lithography; However, these methods are still involved with multi-step manufacturing process including nanolithography of silicon pattern as the pre-step of the soft-lithography.[15,16] Most importantly, glancing angle deposition and similar techniques do not allow in-situ control of size or handedness helical geometries over the production process to attain local photonic patterns on the same substrate.

Direct creation of subwavelength helical metal geometries at the interfaces through spontaneous self-assembly of nanoparticles (NPs) is the holy grail of chiral metasurface production to realize such controllability. However, such process encounters several fundamental barriers especially when we need to ensure strong polarization rotation from plasmonic elements. Firstly, as shown in the typical design of lithographic 3D chiral metasurface patterns, the rotational axis of the self-assembled geometries must be aligned to the surface normal vector to maximize their optical rotatory power.[28] The spontaneous out-of-plane alignment is, however, difficult even for the closely packed interfacial self-assembly of chiral molecules [8,29–34], producing frequent orientational defects[33,34]. It becomes nearly impossible for the plasmonic NP assemblies because such alignment is associated with order of magnitude higher thermodynamic penalties; The stand-up placement of helical geometries on surfaces inevitably leads high potential energy and

mechanical instability. More importantly, unlike closely packed monolayers from chiral molecules,[8,29–34] the empty space between plasmonic elements is a critical requirement to avoid their undesired cross-talk and promote strong polarization effects from in-gap plasmonic resonances. However, the empty space between the nanostructures in self-assembly process is associated with the 'loss' of close-range van der Waals interactions, which make such complex geometries even more thermodynamically unfavorable.

Photon-to-matter chirality transfer offers both simplicity and universality to the chiral synthesis[35,36], suggesting a promising research direction to overcome these fundamental constraints. Here, we report first-ever direct printing of pure metallic nanostructures with 3D chirality on various substrates using circularly polarized light-guided chiral assemblies, realizing single-step mask-free completely solution-processed manufacturing of centimeter-scale chiral matasurface with virtually no spatial or geometrical constraints. The synthesized silver helical assemblies under left- and right-handed circularly polarized light (*L*-CPL and *R*-CPL, respectively) showed distinctive handedness with enantiomeric excess above 80% benefiting from efficient directional assembly starting from the fixed nucleation spot at the liquid-solid interface. The normal incidence of CPL on various solid substrates, for instance, glass, indium titanium oxide (ITO), and polydimethylsiloxane (PDMS), immersed in an aqueous mixture solution of sodium citrate (2.5 mM - 12.5 mM) and silver nitrate (2.5 mM), results in heterogeneous silver nucleation at the liquid-solid interface and the subsequent growth/self-assembly of silver NPs into helicoids array normal to substrate.

The time required for helicoids to form is dependent on light intensity and growth conditions. For most experiments to elucidate growth mechanism of the helicoids in this study, the circularly polarized laser beams were broadened by a set of optical lenses (**Fig. 1a**) while some experimental series were performed with focused lasers to expedite the printing speed. For a

largely broadened 532 nm laser beam with a photon flux of 3.07×10^{21} photons·sec^{-1}·m^{-2}, the helicoid arrays covering an area of *ca* 3.14 cm^2 were produced within 30 minutes, displaying angle-dependent reflective color typical for metasurfaces (**Fig. 1b**; **Fig. S1**). By changing the ellipticity of polarized light (changing angle of quarter-wave plate against the linear polarizer from 5 to 45 degree), the resulted structure showed different circular dichroism (CD) and corresponding g-factor. (**Fig. 1c**,**d**) The *L*-CPL and *R*-CPL illumination of solid substrates results in the growth of right- and left-handed helicoids denoted as Δ- and Λ-enantiomers, respectively (**Fig. 1d-f**). The Δ- and Λ-helicoid arrays displayed strong mirror-symmetrical circular dichroism (CD) spectra with bands at 350, 430, 545, and 780 nm (**Fig. 1g**). Besides glass, the similar arrays with identical polarity were grown on ITO, silicon wafers and PDMS (**Figs. S1** and **S2**).

Different growth stages of helicoids were characterized spectroscopically and imaged by electron microscopy (**Fig. 1h-j, Supplementary Note 1**). After a 5 min exposure, asymmetric dimers of small silver NPs (15-20 nm in diameter) were observed (**Fig. 1h**). The corresponding arrays showed two CD bands in the ultra-violet (UV) and violet parts of the spectrum at 330 and 420 nm with positive and negative signs, respectively (**Fig. 1j**). After a 10 min exposure, vivid helicity of the NP assemblies emerged. The scanning transmission electron microscopy (STEM) images of nanostructure at intermediate growth stage (at 10 min, **Fig. 1i**) revealed that the final complex nanostructures (i.e., **Fig. 1h** at 30 mins) are formed by twisted horseshoe shaped segments consisting of 5-7 NPs with a diameter of 15 – 65 nm. CPL exposure past this 10 min growth time resulted in the formation of vertical stacks of the horseshoe segments. The growth of the helicoid is accompanied by the gradual red shift of the chiroptical bands and emergence of two additional bands for green and near infrared-red wavelengths at 545 and 780 nm, respectively (**Fig. 1j**).

To better understand the photon-to-matter chirality transfer process leading to stand-up helicoidal arrays, a computational model was built utilizing the knowledge about the structure and

shape of the single helicoids obtained from **Fig. 2a**. The observed shape transitions are explained by dynamically changing 'hot-spots' whose positions are determined by the handedness of the incident CPL light. Taking NP dimers as a starting point, exposure to CPL results in an intense electrical field concentrated in different parts of the nanostructure (**Fig. 2b, Supplementary Movies 1** and **2, Supplementary Note 2**), which serves as the attachment points for the site-selective deposition of NPs (**Fig. S3a, Supplementary Movie 3**). The newly added metallic NPs (**Fig. S3b**) will further alter the position of the hot-spots, but they will always be displaced around the rotational axis of the growing helicoid due to the helicity of the incident photon (**Fig. 2c, Supplementary Movie 4**). Indeed, using this iterative process of particle growth, we achieved the twisted horseshoe self-assembled geometry of the intermediate staged helicoids (**V2** in **Fig. 2a**) that matches the experimental geometry (**Fig. 1i**). After this stage, we assumed that the twisted horseshoe shaped chirality motifs are stacked into multi-layers. The simulated CD spectra of the models representing the three different intermediate growth stages (**V1-3**, **Fig 2a**) are nearly identical to the experimental ones, with respect to the polarity of the CD peaks and their spectral placement (**Fig. 2d, Supplementary Note 3**).

Notably, from stage **V2** to **V3**, two additional peaks (star-marked peaks in **Fig. 2d**) appeared as we found in the experimental data. To prove that these new peaks are originated from the stacking of the twisted horseshoe (TH) segments on top of each other, we further simplified the computational models (**Fig. 2e**) and investigate their electromagnetic resonance modes by comparing calculated extinction spectra of single- and double-layered structures (**Supplementary Note 4**). The evolution of the calculated difference in extinction cross section under *L*- and *R*-*CPL* from single- to double-layer clearly shows the splitting of resonance peak and matched with experimental observation **(Fig. 2f,g)**. Each of the two resonance mode of a single-layer (at 400 and 525 nm, respectively) into two, generating the four resonance modes in total once the double-

layered structures are formed. To visualize different resonance modes, the volume arrow plots of current density of both single and double layered TH were analyzed at their resonance wavelengths (**Fig. 2h,i**). While the single layer TH shows two (bonding and anti-bonding type of plasmon coupling, respectively) modes in a single solid domain, additional resonance modes were found in double layered TH due to inter-layer coupling.

The chiroptical scattering from the helicoids is strong enough for showing selective reflection of CPL as shown in the iridescent metallic chiral green beetle, *Chrysina gloriosa* [37] (**Fig. S4a**); The surface exposed to *L*-CPL for 15 min (Δ-helicoids metasurface) start to have visible color/brightness variations under LCP and RCP filters as the chiral green beetles do (**Fig. S4b**). For further investigation of such scattering dissymmetry from helicoids, we conduct the statistical analysis on single-particle scattering spectroscopy. We placed Δ- and Λ-helicoid samples prepared on cover slide (**Fig. S5**) under a randomly polarized focused laser beam at wavelength of 488 nm and analyzed single-particle circularly polarized luminescence (see **Supplementary note 5** and **Fig. S6** for the details). As expected, single helicoids with different handedness displayed distinctly different circular polarizations (**Fig. 3a**). The average dissymmetry *g*-factor reached as high as −0.33 for the Δ-helicoids, indicating that they scatter *R*-CPL stronger than *L*-CPL, and vice versa for Λ-helicoids: $g = +0.15$ while achiral sphere shows nearly zero asymmetry factor (**Fig. 3b, Supplementary Table 2**). The repeated observation of the scattered CPL intensities from single Δ-helicoid compared to achiral nanosphere control over a hundred imaging frames demonstrates not only polarity selective scattering but also their robustness and photostability (**Fig. 3c,d**).

The simplicity of CPL-induced formation of the chiral plasmonic nanostructures is a promising pathway to develop direct printing system of metasurface patterns. Employing a programmable moving stage for the 532 nm laser beam with 0.36 mm spot size (**Fig. 4a**), we

created patterns of discrete small dots alternating translation and illumination (**Fig. 4b, Fig. S7a, Supplementary Note 6**). The focused beam (photon flux: 9.48×10^{24} photons·sec^{-1}·m^{-2}) was parked for 30 seconds before translation to create a patterned surface with 1 mm diameter. We then further demonstrated continuous printing during the movement of the stage (stage moving speed: 1.1 mm/sec) by fabricating two rows of letter patterns with *R*-CPL and *L*-CPL for the first and second row, respectively (**Fig. 4c**, **Fig. S7b**, printing demo recording found in **Supplementary Movie 5**). The strong chiroptical band at 500 nm in the CD spectra from these two rows have opposite signs (**Fig. 4d**). Analysis of these two rows by microscale Mueller matrix polarimetry (MMP) **(Figs. S8-11**) also confirmed a complete set of polarization parameters and high-contrast polarization from the patterns. To show application of the printed chiral metasurface patterns in polarization-encryption, we printed the Greek letter χ (as in χειρ, i.e. 'hand') and its mirror image on the same substrate using *L*-CPL and *R*-CPL, respectively (**Fig. 4e, Fig. S7c**). The circular birefringence satisfied the Kramers–Kronig relation with the CD spectrum and confirmed high rotational power of the helicoid arrays (**Fig. 4f**). The maps of the Mueller matrix elements acquired for the prominent 500 nm band in the CD spectrum were obtained for the sample area of 5.2 cm by 9.2 cm (**Fig. 4g-j**, **Supplementary Note 6**). The images obtained for lasers with different polarization rotation vividly showed negative and positive CD and *g*-factors in MMP maps.

Consistent with the chirality transfer determined by the spin angular momentum of the photons, the maximum of the chiroptical response of the silver helicoids were dependent on the wavelength of light source (**Fig. 5a**). The required photon flux to form silver helicoid patterns can be as low as of 9.74×10^{20} photons·sec^{-1}·m^{-2} when the broadened 405 nm laser source was used. Although 660 nm is far off from the resonance of small silver NPs, the CPL illumination can still successfully produce the superstructures but at a slower rate (**Supplementary Note 7**). The SEM images of the resulting structures under different wavelengths of light source showed that longer

wavelengths form bigger helicoids (**Fig. 5c**). The electromagnetic simulation results from the helicoid model based on the experimental structural parameters of these three superstructures also show spectral range changes in their chiroptical bands (**Fig. 5b,d, Fig. S13 and S14,** and **Supplementary Note 7**).

The handedness, wavelength and power density of the laser beam can be easily varied while we print the patterns in different parts of the substrates. Such flexibility gives the possibility of fast and versatile printing of integrated multi-grid or compartment patterns with various local geometries, which lithographic methods can hardly provide. To show on-the-fly tunability of the chiroptical activity of local patterns, we printed 24 different grid spots with 1 mm diameter by two-step exposure of different combinations of light source handedness, *L*-CPL or *R*-CPL, and wavelength, 405, 532, or 660 nm (**Fig. 5e**, **Supplementary Note 8**). The resulting CD (**Fig. S15**) and optical rotatory dispersion (ORD, **Fig. S16**) spectra show that their chiroptical spectra can be modulated in the range of full visible wavelength (**Fig. 5f**,**g, Tables S3** and **S4**). The optical rotatory power from the helicoid model was also demonstrated using finite-difference time-domain (FDTD) simulations (**Fig. S17**, **Supplementary Note 9**). To demonstrate the applicability of our technique in sensing, we adopt our plasmonic helicoid pattern for chiral analytes, Pepsin, sensing based on CD peak wavelength shift (**Fig. 5h-j**). The CD spectra gradually red shifted with increase in Pepsin concentration and the limit of detection can be reach below 100 pM (**Fig. 5j**). We also confirmed the enantiomer selectivity of the system through the different absolute shift observed upon absorption of *L*-and *D*- lysine on Λ-helicoids (**Fig. S18**).

The proof-of-principle data for polarization-encryption and sensor manufacturing clearly showed the potential application of printing system in both informatics and diagnostics. Especially, our technique can print the distinguishable local patterns with various chirality using reduced the

effective printing area by four order of magnitude (compared with spot diameter of 2 cm in **Fig. 1b**), which asserts the inherent scalability of our method. We believe that with further development including a precise focal point adjustment procedure, the technique could provide a higher patterning resolution. The easy access to this simple printing technique will allow customizing many common optical lab supplies that are intensively in use by communities outside of metamaterials, exemplified by multi-well microplates plates for high throughput chiroptical analysis (**Fig. S19a**). More importantly, the successful printing of miniaturized multi-grid patterns with various combinational local patterns (**Fig. S19b**) suggests potential development of the chiroptic-based diagnostic sensing system with the higher selectivity than currently available CD based sensing technology. For instance, the combinational chiroptical activity changes of the 24 different helicoids patterns (**Fig. 5e-g**) will provide a unique footprint for the specific analyte as each of 24 chiral elements will react differently (as exemplified in the insets of **Fig. S19b**). The continuous patterning ability of our technique shown in **Fig. 4c** could also allow direct printing of the chiral metallic channel in microfluidic channel and sped up applications of metasurface as an in-line analysis tool for continuous flow microreactors (**Fig. S19c**), which can be used for the study of various chemical reactions that lead to a change of the CD spectrum of the sample. Finally, it should be also emphasized the fact that the suggested printing procedure is not involved with any organic ligand materials, which can provide better sensitivity to its dielectric environment, but also eliminate charge transport dilemma of solution-processed nanomaterials that often hinders their practical application in electrochemical, photocatalytic and optoelectronic devices.[38]

In conclusion, chirality of incident photons can be successfully transferred to the chirality of nanostructures assembled at liquid-solid interfaces in a way their rotational axis is aligned to the surface normal of the substrate, which enables high chiroptical activity and *g*-factors. The technique was solution processed under ambient conditions and enables rapid large area patterning

of wide range of substrates. The chiral plasmonic metasurfaces that can be used for photonic, optoelectronic, and electromechanical devices. Particular benefits are expected for wearable biosensing devices for multiparameter health monitoring based on chiral spectroscopies of chiral metabolites that require macroscale patterns with different photonic activity. The method may also be suitable for non-metallic but still optically active nanostructures,[36,39] combined with currently available light-induced additive manufacturing process to create hierarchical nanostructures with multi-scale chirality.

Methods

Synthesis of silver helicoids on substrates. The thin PDMS substrate in **Fig. S2** was prepared using a PDMS mixture (PDMS curing agent mix (1:10), Dow Corning, US) spun on a silicon mold at 1,000 rpm for 30 seconds, followed by incubation at 70 °C for 2 h. To synthesize the silver helicoids, silver nitrate ($AgNO_3$, Cat.# 209139) and trisodium citrate dihydrate (Cat.# S4641) were purchased from Sigma-Aldrich (Milwaukee, WI). Ultrapure water from a Direct-Q3 system (18.2 MΩ·cm, Millipore; Billerica, MA) was used in this work., the desired substrate (either glass, indium tin oxide (ITO)/glass, polydimethylsiloxane (PDMS), or silicon) was submerged in a solution of silver precursor ($AgNO_3$, 2.5 mM) and citrate (12.5 mM), while the height from substrate to surface of the solution was fixed at 3 cm. Three different lasers (wavelength of 405, 532, and 660 nm), modulated to emit either left- or right-circularly polarized light (*L*-CPL and *R*-CPL, respectively), were directed perpendicular to the substrate with varying power density for different time up to 30 minutes depending on purpose of experiments. The patterned substrates were immersed in clear DI water solution and washed three times before optical or imaging analysis.

Optical set-up for CPL-induced centimeter-scale patterning of surfaces with helicoids. The diode-pumped continuous wave lasers with three different wavelengths of 405, 532, and 660 nm (CrystaLaser, NV, USA) were used as light sources. The laser emissions were broadened into spots with a diameter of 1-2 cm using a combination of Plano-concave and -convex lenses (**Fig. 1a**).

The broadened beams were transformed to CPL by directing it through a linear polarizer and a quarter-wave plate. Since the quarter-wave plate is made with a birefringent material, the linearly polarized light turned to CPL by passing through the quarter-wave plate with the 45° transmission angle. By rotating the quarter-wave plate 90° relative to the previous angle, the handedness of the CPL can be changed.

Circular dichroism spectroscopy. The helicoid structures for optical analysis were created on cover glass with a size of 22x22 mm and thickness of 1.5 mm. Circular dichroism (CD) spectra of the samples were obtained using a Jasco J-815 or J-1700 CD spectrometer equipped with one PMT detector in 200-800 nm range and two InGaAs near infrared (NIR) detectors in 800-1600 nm and 1600-2500 nm range. The CD spectra were measured with the typical scanning parameters: scanning speed, 500 nm/min; data pitch, 1 nm; bandwidth, 5 nm (NIR bandwidth, 10 nm); digital integration time, 0.25 s; and one accumulation.

Mueller matrix polarimetry. Mueller matrix polarimetry (Hinds instrument) was used to obtain a 4 x 4 Mueller Matrix (**M**). Briefly, a total of four photoelastic modulators (PEMs) were employed to extract **M** from the samples; 2 of them were for a polarization state generator and the rest of them were for a polarization state analyzer. As described elsewhere,[40,41] four input Stokes vectors generated by PEMs of the polarization state generator and four output vectors analyzed by PEMs of analyzer resulting in a matrix of 16 measured light intensities that can be directly used to determine 16 elements of the **M** of the sample. The optical parameters (horizontal linear dichroism (LD), 45° linear dichroism (LD'), horizontal linear birefringence (LB), 45° linear birefringence (LB'), circular dichroism (CD), circular birefringence (CB)) were consequently extracted from the **M**.

Electron microscopy. Scanning electron microscopy (SEM) samples were prepared as described above by using ITO coated glass slides (Nanocs Inc) as substrates, followed by drying at room temperature. After checking their CD spectra, SEM imaging on samples were performed in FEI Nova NanoLab Dual Beam SEM and FEI Helios Nanolab at 5 kV accelerating voltage and 0.4 nA beam current under secondary electron detection mode. Scanning transmission electron microscopy (STEM) samples were prepared on PDMS and transferred to a copper grid coated with holey carbon supported on a continuous carbon film (TedPella 01824) by stamping technique.

Simultaneous imaging with three different detectors were performed with FEI Helios Nanolab at 29 kV accelerating voltage.

Single-particle circularly polarized luminescence measurements. Silver helicoids were prepared on glass coverslips and imaged by single-particle spectroscopy under 488 nm continuous wave (CW) randomly polarized light (excitation intensity: 3.87×10^5 mW/cm^2). The emission polarization was analyzed with a liquid crystal variable retarder (Thorlabs LCC1223T-A). See **Supplementary Note 1** for detailed methods.

Electromagnetic computation. To elucidate the growth mechanism and chiroptical evolution of the silver helicoids, the electromagnetic computations were performed using finite-element-analysis (FEA) software, COMSOL Multiphysics 5.5. See **Supplementary Notes 3** and **4** for detailed methods. The chiroptical change in helicoid structures with different sizes were evaluated by constructing 3D models based on Table S1 and electromagnetic simulation by finite-difference time-domain method (FDTD) utilizing the commercial software Lumerical. See **Supplementary Note 7** for details. The similar FDTD analysis were performed to evaluate the optical rotatory power of the helicoid structures for linearly polarized light. See **Supplementary Note 9** for detailed method and discussion.

Printing and patterning of chiral metasurfaces. The CPL-induced chiral metastructure printing was demonstrated with a prototype printing set up equipped with a motorized sample stage (Zaber Technology, Inc.). The customized Matlab code was used for pixelating imported images and programming the sample stage movement corresponding to ***x-y*** coordinates of pixelated images shown in **Fig. S7**. See **Supplementary Note 6** for more details.

Biosensing experiments with chiral metasurface patterns. The circular Λ -helicoids metasurface pattern with 1 cm diameter was printed on cover slides. Lyophilized (salt-free) Pepsin (Cat.# , 10108057001) and *L*- and *D*-lysine (Cat.#, L8021) were purchased from Sigma-Aldrich and dissolved in DI water with various concentrations. The CD spectra of printed pattern were measured after addition of 10 μL of analyte solutions were added with cover slip.

Acknowledgments: The central part of the funding came from the Vannevar Bush DoD Fellowship to N.A.K. titled "Engineered Chiral Ceramics" ONR N000141812876 and ONR COVID-19 Newton Award "Pathways to Complexity with `Imperfect' Nanoparticles" HQ00342010033. Authors acknowledge additional funding came from National Science Foundation Grant CHE-1807676 to J.S.B as well as Office of Naval Research (MURI N00014-20-1-2479); AFOSR FA9550-20-1-0265, Graph Theory Description of Network Material The central part of this work was supported by the NSF project "*Energy- and Cost-Efficient Manufacturing Employing Nanoparticles*". Michigan Center for Materials Characterization $(MC)^2$ is acknowledged for its assistance with electron microscopy, and for the NSF grant #DMR-9871177 for funding of the JEOL 2010F analytical electron microscope used in this work.

Author contributions: N.A.K. and J.-Y.K. designed the project. J.-Y.K. built the experimental set-up. J.-Y.K. performed the helicoid formation studies under different light ellipticity with assistant from S.K. J.-Y.K. and C. M. synthesized and characterized library of helicoids with assistance from M.C. J.-Y.K. and C. M. measured CD data. J.-Y.K. and M.C. built the auto motorized stage system for printing demo. Z. J.P. and J. B. characterized chiroptical properties from single particle analysis. J.-Y.K. conducted SEM and STEM imaging with assistance from E.S.T.E. J.-Y.K. measured Mueller matrix with assistance from W.C. J.-Y.K. manufactured the encrypted images with helicoids and mapped under the Mueller polarimetry. M.C. processed image data from Mueller polarimetry. J-Y.K. performed the FEA and FDTD simulations. J-Y.K. and E.S.T.E conducted biosensing experiments. J.-Y.K. and N.A.K. wrote the first draft and all authors contributed to data analysis, discussion, and writing.

Competing interests: Authors declare that they have no competing interests.

Data and materials availability: All data are available in the main text or the supplementary materials.

Supplementary Materials

Supplementary Notes (Supplementary Note 1-9)

Supplementary Figures (Figs. S1-19)

Tables S1 to 4

References (1–4)

Supplementary Movies 1 to 5

References

1. Guerrero-Martínez, A., Grzelczak, M. & Liz-Marzán, L. M. Molecular Thinking for Nanoplasmonic Design. *ACS Nano* **6**, 3655–3662 (2012).
2. Valev, V. K. *et al.* Nonlinear superchiral meta-surfaces: Tuning chirality and disentangling non-reciprocity at the nanoscale. *Adv. Mater.* **26**, 4074–4081 (2014).
3. Guerrero-Martínez, A., Alonso-Gómez, J. L., Auguié, B., Cid, M. M. & Liz-Marzán, L. M. From individual to collective chirality in metal nanoparticles. *Nano Today* **6**, 381–400 (2011).
4. Hentschel, M., Schäferling, M., Duan, X., Giessen, H. & Liu, N. Chiral plasmonics. *Science Advances* (2017) doi:10.1126/sciadv.1602735.
5. Chen, W. *et al.* Nanoparticle superstructures made by polymerase chain reaction: Collective interactions of nanoparticles and a new principle for chiral materials. *Nano Lett.* **9**, 2153–2159 (2009).
6. Ma, W. *et al.* Chiral Inorganic Nanostructures. *Chem. Rev.* **117**, (2017).
7. Valev, V. K., Baumberg, J. J., Sibilia, C. & Verbiest, T. Chirality and chiroptical effects in plasmonic nanostructures: Fundamentals, recent progress, and outlook. *Adv. Mater.* **25**, 2517–2534 (2013).
8. Maoz, B. M. *et al.* Amplification of Chiroptical Activity of Chiral Biomolecules by Surface Plasmons. *Nano Lett.* **13**, 1203–1209 (2013).
9. Ben-Moshe, A. *et al.* Enantioselective control of lattice and shape chirality in inorganic nanostructures using chiral biomolecules. *Nat. Commun.* **5**, 4302 (2014).
10. Govorov, A. O. *et al.* Chiral nanoparticle assemblies: circular dichroism, plasmonic interactions, and exciton effects. *J. Mater. Chem.* **21**, 16806 (2011).
11. Wang, Z., Cheng, F., Winsor, T. & Liu, Y. Optical chiral metamaterials: A review of the fundamentals, fabrication methods and applications. *Nanotechnology* vol. 27 412001 (2016).
12. Guan, Y. *et al.* Chiral plasmonic metamaterials with tunable chirality. *ACS Appl. Mater. Interfaces* **12**, 2021 (2020).
13. Frank, B. *et al.* Large-area 3D chiral plasmonic structures. *ACS Nano* **7**, 6321–6329 (2013).
14. Cai, J. *et al.* Polarization-sensitive optoionic membranes from chiral plasmonic nanoparticles. *Nat. Nanotechnol.* (2022) doi:10.1038/s41565-022-01079-3.
15. Kim, R. M. *et al.* Enantioselective sensing by collective circular dichroism. *Nature* **612**, 470–476 (2022).
16. Namgung, S. D. *et al.* Circularly polarized light-sensitive, hot electron transistor with chiral plasmonic nanoparticles. *Nat. Commun.* **13**, 5081 (2022).
17. Gansel, J. K. *et al.* Tapered gold-helix metamaterials as improved circular polarizers. *Appl. Phys. Lett.* **100**, 101109 (2012).
18. Kaschke, J. & Wegener, M. Gold triple-helix mid-infrared metamaterial by STED-inspired laser lithography. *Opt. Lett.* **40**, 3986 (2015).

19. Gansel, J. K. *et al.* Gold helix photonic metamaterial as broadband circular polarizer. *Science* **1513**, 1513–1515 (2009).

20. Esposito, M. *et al.* Three dimensional chiral metamaterial nanospirals in the visible range by vertically compensated focused ion beam induced-deposition. *Adv. Opt. Mater.* **2**, 154–161 (2014).

21. Esposito, M. *et al.* Triple-helical nanowires by tomographic rotatory growth for chiral photonics. *Nat. Commun.* **6**, 1–7 (2015).

22. Esposito, M. *et al.* Nanoscale 3D chiral plasmonic helices with circular dichroism at visible frequencies. *ACS Photonics* **2**, 105–114 (2015).

23. Ma, W. *et al.* Attomolar DNA detection with chiral nanorod assemblies. *Nat. Commun.* **4**, 2689 (2013).

24. Hou, Y. *et al.* Ultrabroadband Optical Superchirality in a 3D Stacked-Patch Plasmonic Metamaterial Designed by Two-Step Glancing Angle Deposition. *Adv. Funct. Mater.* **26**, 7807–7816 (2016).

25. Singh, J. H., Nair, G., Ghosh, A. & Ghosh, A. Wafer scale fabrication of porous three-dimensional plasmonic metamaterials for the visible region: Chiral and beyond. *Nanoscale* **5**, 7224–7228 (2013).

26. Gibbs, J. G., Mark, A. G., Eslami, S. & Fischer, P. Plasmonic nanohelix metamaterials with tailorable giant circular dichroism. *Appl. Phys. Lett.* **103**, 213101 (2013).

27. Kilic, U. *et al.* Broadband Enhanced Chirality with Tunable Response in Hybrid Plasmonic Helical Metamaterials. *Adv. Funct. Mater.* **31**, 2010329 (2021).

28. Lee, H. E. *et al.* Cysteine-encoded chirality evolution in plasmonic rhombic dodecahedral gold nanoparticles. *Nat. Commun.* **11**, 1–10 (2020).

29. Bejarano-Villafuerte, Á. *et al.* A Chiral Self-Assembled Monolayer Derived from a Resolving Agent and its Performance as a Crystallization Template for an Organic Compound from Organic Solvents. *Chem. – A Eur. J.* **18**, 15984–15993 (2012).

30. Lalander, C. H., Zheng, Y., Dhuey, S., Cabrini, S. & Bach, U. DNA-Directed Self-Assembly of Gold Nanoparticles onto Nanopatterned Surfaces: Controlled Placement of Individual Nanoparticles into Regular Arrays. *ACS Nano* **4**, 6153–6161 (2010).

31. Barrow, S. J., Wei, X., Baldauf, J. S., Funston, A. M. & Mulvaney, P. The surface plasmon modes of self-assembled gold nanocrystals. *Nat. Commun.* **3**, 1275 (2012).

32. Thacker, V. V *et al.* DNA origami based assembly of gold nanoparticle dimers for surface-enhanced Raman scattering. *Nat. Commun.* **5**, 3448 (2014).

33. Murphy, J. N., Cheng, A. K. H., Yu, H.-Z. & Bizzotto, D. On the Nature of DNA Self-Assembled Monolayers on Au: Measuring Surface Heterogeneity with Electrochemical in Situ Fluorescence Microscopy. *J. Am. Chem. Soc.* **131**, 4042–4050 (2009).

34. Herne, T. M. & Tarlov, M. J. Characterization of DNA Probes Immobilized on Gold Surfaces. *J. Am. Chem. Soc.* **119**, 8916–8920 (1997).

35. Kim, J. Y. *et al.* Assembly of Gold Nanoparticles into Chiral Superstructures Driven by Circularly Polarized Light. *J. Am. Chem. Soc.* **141**, 11739–11744 (2019).

36. Yeom, J. *et al.* Chiral templating of self-assembling nanostructures by circularly polarized light. *Nat. Mater.* **14**, 66–72 (2015).

37. Choi, W. J. *et al.* Terahertz circular dichroism spectroscopy of biomaterials enabled by kirigami polarization modulators. *Nature Materials* vol. 18 820–826 (2019).

38. Kim, J. Y. & Kotov, N. A. Charge transport dilemma of solution-processed nanomaterials. *Chemistry of Materials* vol. 26 134–152 (2014).

39. Srivastava, S. *et al.* Light-controlled self-assembly of semiconductor nanoparticles into twisted ribbons. *Science (80-.).* **327**, 1355–1359 (2010).

40. Arteaga, O., Freudenthal, J., Wang, B. & Kahr, B. Mueller matrix polarimetry with four photoelastic modulators: Theory and calibration. *Appl. Opt.* **51**, 6805–6817 (2012).

41. Arteaga, O. & Kahr, B. Mueller matrix polarimetry of bianisotropic materials [Invited]. *J. Opt. Soc. Am. B* **36**, F72 (2019).

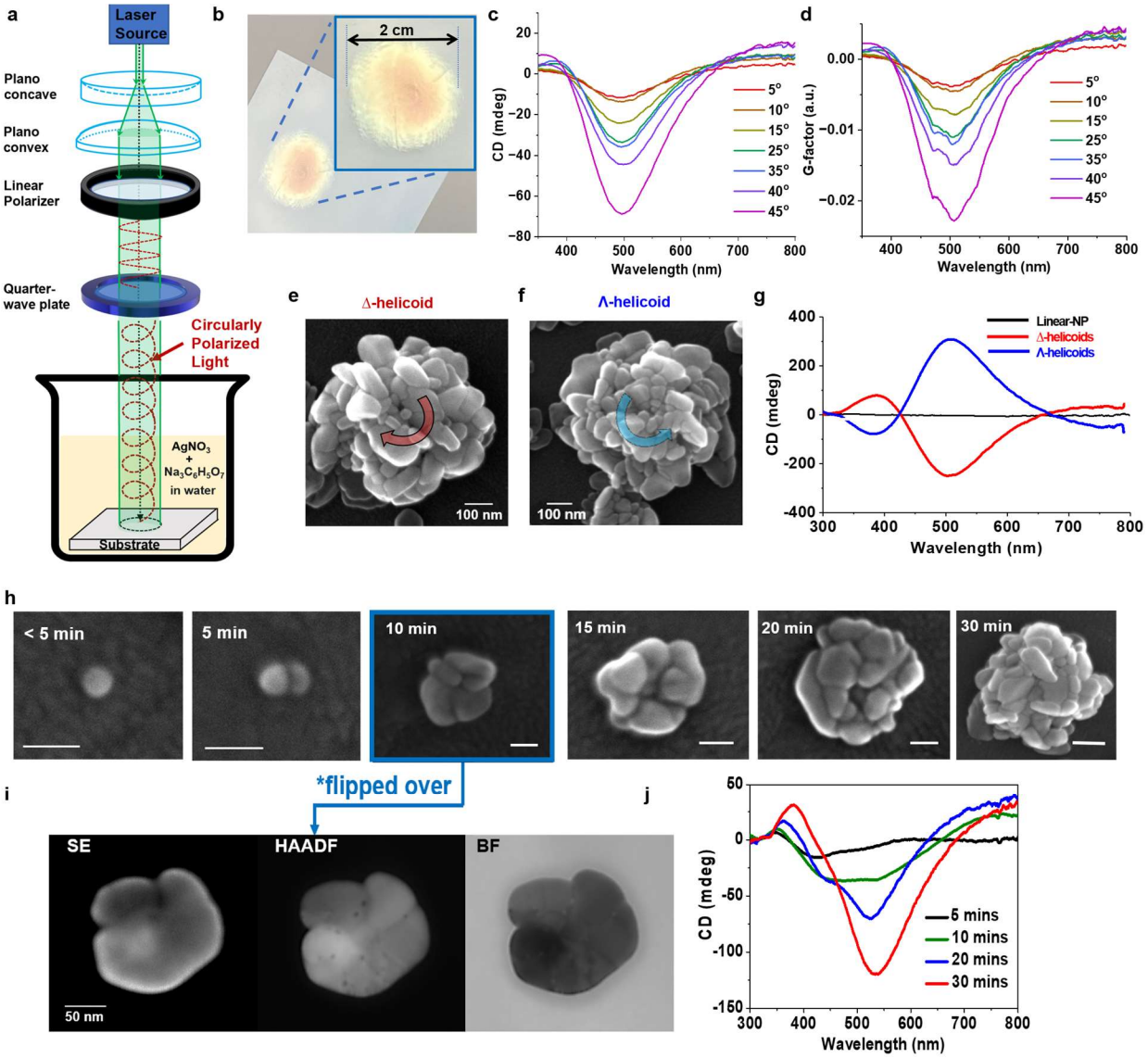

Figure 1. Formation of nanostructured silver helicoids with out-of-plane substrate alignment driven by the circularly polarized light (CPL). (a) Schematic description of experimental set up for CPL driven synthesis of silver helicoids **(b)** Photograph of silver helicoids printed on glass substrate in reflective angle. **(c)** Circular dichroism (CD) and **(d)** g-factor of silver helicoids synthesized by different ellipticity (changing angle between linear polarized light and quarter-wave plates from 5 to 45 degree) of the polarized light. **(e, f)** Scanning electron microscope (SEM) image of Δ-helicoids and Λ-helicoid formed on ITO/glass by *L*-CPL and *R*-CPL, respectively. **(g)** CD spectra of Δ- or Λ-helicoids formed on glass substrates after 30-min exposure to *L*-CPL and *R*-CPL, respectively. Δ-helicoids grow under *L*-CPL and Λ-helicoids grow under *R*-CPL. **(h-j)** Experimental observation of different growth stages of Δ-helicoids. (h) SEM images of Δ-helicoids at different illumination times of *L*-CPL. The scale bar is 50 nm. (i) STEM images of Δ-helicoid at 10 min growth stage. Secondary electron (SE), high-angle annular dark-field (HAADF), and bright field (BF) detectors are used simultaneously to see the rotational structure. Note that the structure is transferred from the original substrate to the transmission electron microscopy (TEM) grid and thus flipped over on the grid. (j) CD spectra of silver helicoids in different growth stages.

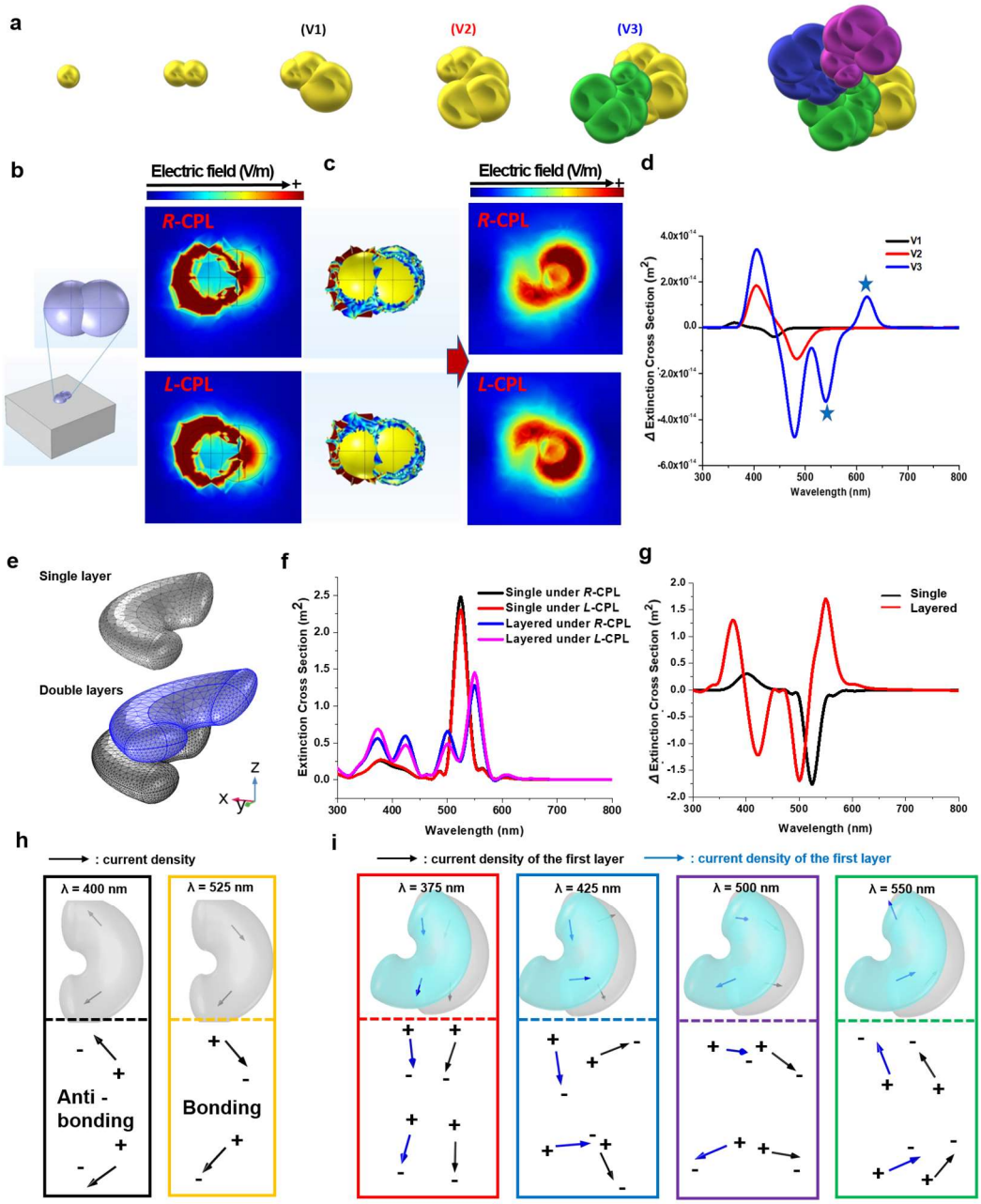

Figure 2. Computational analysis of different growth stage of Δ-helicoids. **(a)** 3D computational models built based on electromagnetic simulation of dynamic 'hot spots' under illumination with *L*-CPL for silver deposition and assembly. **(b)** Dimer model on substrate (left) and asymmetric cross sectional (left) electric field distribution on the dimer under *R*-CPL (top) and *L*-CPL (bottom), respectively. **(c)** The asymmetric nanostructure model at the next preceding growth stage (left) predicted from the electric field volume plot in (b) and the subsequent cross sectional electric field distribution on it**. (d)** Calculated differential extinction cross section of *L*-CPL to *R*-CPL (Δ Extinction cross section) spectra of the three different models (**V1-3**). (**e-i)** electromagnetic models for multi-layered structure in Δ-helicoids. (e) Twisted horseshoe models that represent two different growth stages in (a) (single layer: **V2**; double layers: **V3**). (f) Calculated extinction cross sections of the single and stacked twisted horseshoe model under *L*-CPL and *R*-CPL. (g) Δ Extinction cross section for the twisted horseshoe model**.** Current density flow map of (h) single and (i) twisted horseshoe models at different resonance modes.

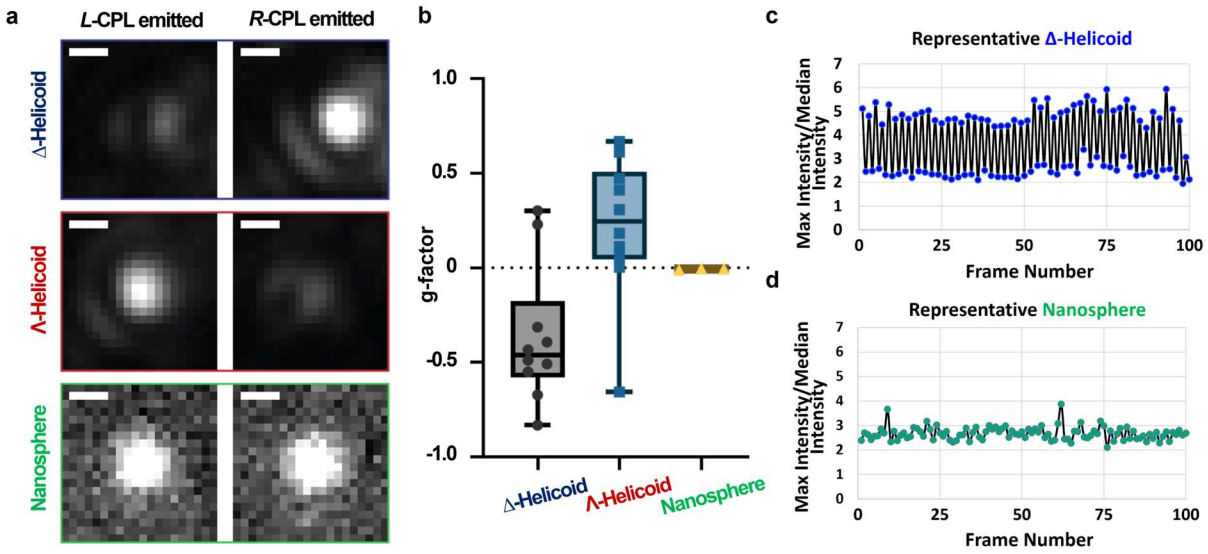

Figure 3. Single-particle analysis of chiroptical scattering from silver helicoids on substrate. **(a)** Single-particle optical microscopy images of Δ-helicoids, Λ-helicoid, and nanosphere during collection of *L*-CPL (left) or *R*-CPL (right) scattering upon excitation with randomly polarized 488-nm continuous wave laser light (scale bars: 250 nm); (**b**) Dissymmetry g-factor for Δ- and Λ-helicoids and achiral nanosphere. Each point is a single-particle measurement. The control experiment with achiral nanosphere shows nearly zero asymmetry factor. (c) Repeated observations of the max intensity/median intensity of scattered light from a single Δ-helicoid and achiral nanosphere (Odd frames: *R*-CPL detection; Even frames: *L*-CPL detection).

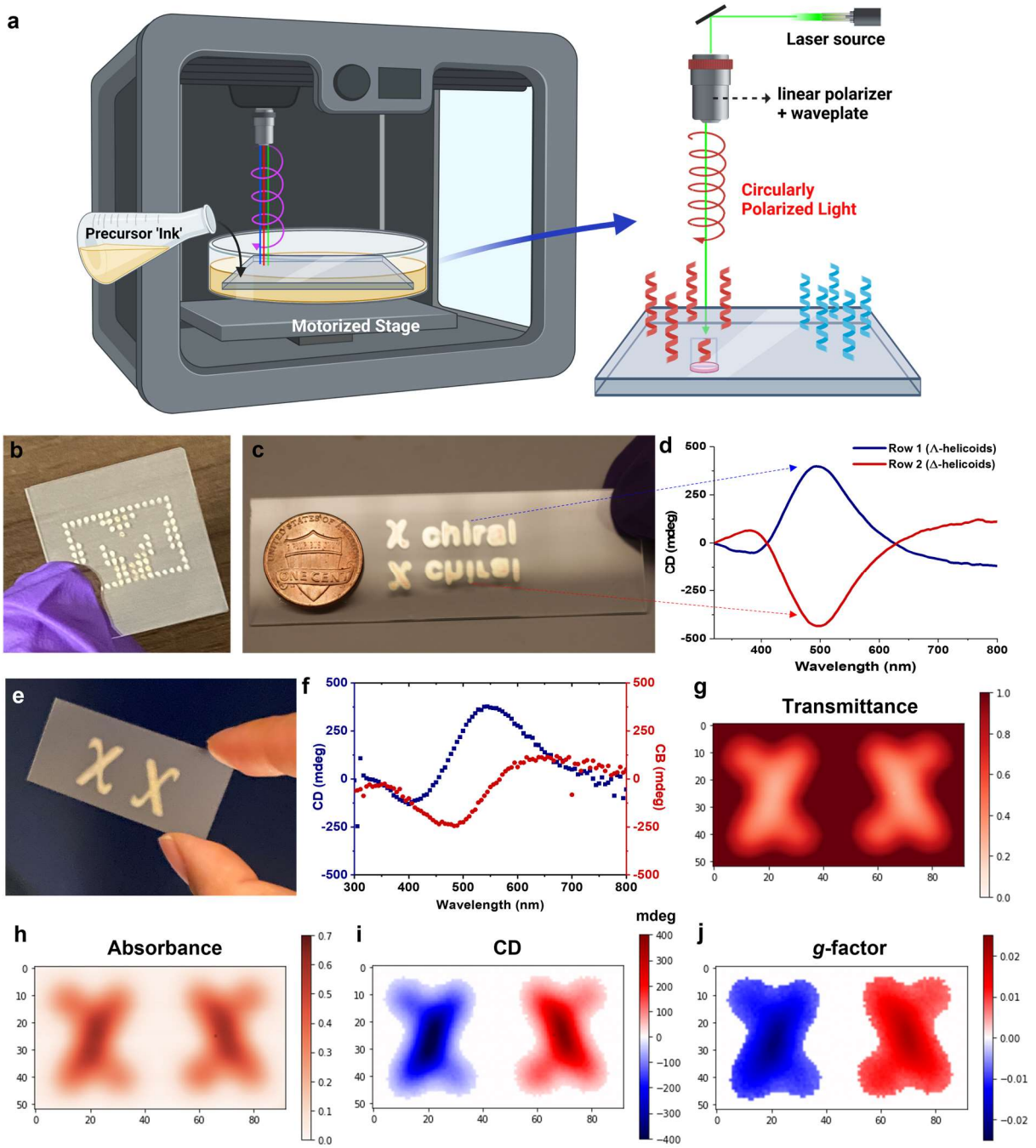

Figure 4. Direct printing of chiral metasurfaces. (a) Schematic description of chiral metastructure printing system with motorized stage. **(b)** The photograph of grid pattern on glass substrate. (**c**) The photograph of continuous writing structures formed by *R*-CPL (upper row) and *L*-CPL (lower row) 532 nm lasers and their **(d)** CD spectra. **(e-j)** Two mirrored letter, 'χ', printed by 532 nm *L*-CPL (left) and *R*-CPL (right), respectively. (e) Photograph of the sample. (f) CD and CB spectra of Λ-helicoid pattern measured by Mueller matrix polarimetry. (g) Transmittance, (h) Absorbance, (i) CD, and (j) *g*-factor map of the whole pattern obtained by Mueller matrix polarimetry with spatial resolution of 1 mm.

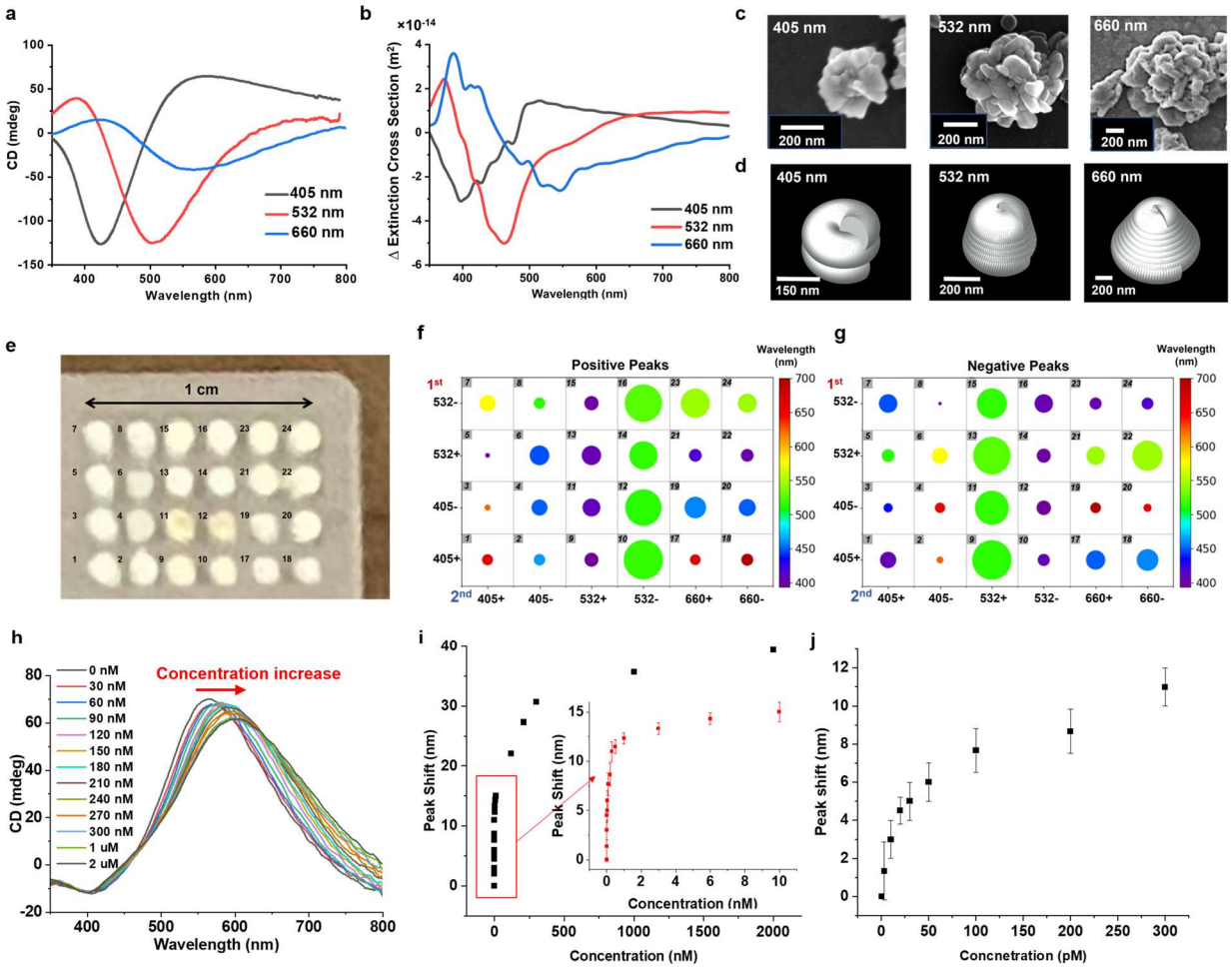

Figure 5. Helicoids formed with various CPL sources with different wavelengths and sensor application. (**a-d**) Δ-helicoids manufactured under three different wavelengths. (405, 532, and 660 nm) (a) Experimental CD spectra and (b) calculated differential extinction cross section of (d) 3D Δ-helicoid models; The model built based on the experimental geometry parameters observed in (c) SEM images of Δ-helicoids synthesized by three different wavelength. **(e)** Photograph of miniatured grid patterned library demo with various bi-layered structures manufactured under 24 different combinations of ellipticity and wavelengths of light source. **(f, g)** The color and intensity map of positive (f) and negative (g) CD peaks of the bi-layered library samples showed in Fig. 5e (Legend: *wavelength of CPL* used to manufacture for 1st layer and 2nd layer; + and - corresponds to *L*-CPL and *R*-CPL, respectively; The diameter of bubble plot is proportional to intensity; Full CD and ORD spectra, and the CD peak readout data of each sample numbered with gray boxed label is available in **Fig. S15, S16** and **Table S3. (h-j)** Detection of Pepsin using CD change in Λ-helicoids metasurface. (h) CD spectra change in increase of concentration of Pepsin. CD peak change plot with increase of concentration of Pepsin in the range of (i) 0 to 2 μM and (j) their low concentration region (0 to 300 pM). All the error bars shown in this figure are standard deviation based on the measurements of 3 sets of samples.